Image-based PSF Estimation for Ultrasound Training Simulation

Oliver Mattausch and Orcun Goksel

Computer-assisted Applications in Medicine Group, ETH Zurich, Switzerland

Abstract. A key aspect for virtual-reality based ultrasound training is the plausible simulation of the characteristic noise pattern known as ultrasonic speckle. The formation of ultrasonic speckle can be approximated efficiently by convolving the ultrasound point-spread function (PSF) with a distribution of point scatterers. Recent work extracts the latter directly from ultrasound images for use in forward simulation, assuming that the PSF can be known, e.g., from experiments. In this paper, we investigate the problem of automatically estimating an unknown PSF for the purpose of ultrasound simulation, such as to use in convolution-based ultrasound image formation. Our method estimates the PSF *directly* from an ultrasound image, based on homomorphic filtering in the cepstrum domain. It robustly captures *local* changes in the PSF as a function of depth, and hence is able to reproduce *continuous* ultrasound beam profiles. We compare our method to numerical simulations as the ground truth to study PSF estimation accuracy, achieving small approximation errors of $\leq 15\%$ FWHM. We also demonstrate simulated in-vivo images, with beam profiles estimated from real images.

1 Introduction

Ultrasound is a relatively low-cost and risk-free medical examination modality. The existence of various ultrasound-specific artifacts necessitate extensive training of sonographers, since standard examination procedures like the assessment of the gestational age of an embryo can lead to a life or death decision in the face of a possible abortion. It was suggested in [17] that medical students have a chance to learn only 80% of the important pathologies after one year of education. These show the enormous untapped potential of virtual-reality based simulation of ultrasound examination to boost the success rate of medical procedures, where arbitrary scenes, pathologies, and embryo instances can be simulated.

One aspect of ultrasound (US) interaction with tissue is through its scattering by sub-wavelength tissue structures and particles, herein called *scatterers*. This interaction creates the typical interference patterns known as ultrasonic speckle. Speckles can be efficiently approximated by convolving a point-spread-function (PSF) with said scatterers [2, 13, 5]. The interactions of the US beam with macro-level surfaces (comparable or larger than wavelength) can be simulated, e.g., using fast ray-tracing methods at interactive rates [4]. An inverse-problem approach of reconstructing scatterer parametrizations based on speckle

observations was proposed [11], such that plausible images of the observed tissue can be generated in simulations from its a-priori imaging examples. One of the major standing issues with inverse-problem scatterer reconstruction, however, is the point-spread-function (PSF) being unknown in general. The same is true for convolution-based image simulation, where the knowledge of PSF is also required as a fundamental input parameter.

While PSF estimation has been studied thoroughly in the context of blind deconvolution for improving US image fidelity, to the best of our knowledge it has not been investigated before in the context of ultrasound image simulation for training. Currently, the state-of the-art [2, 13, 5, 4, 11] is to manually define and hand-craft a PSF, which is tedious technique, also not generalizable for changing imaging parameters. A PSF estimation method for the limited case of 1D deconvolution and minimum phase signals in the *cepstrum domain* has been introduced for ultrasound by Jensen et al. [8] and applied to in-vivo data [7]. The more general case of non-minimal signals typically require the solution of an ill-posed phase unwrapping problem [18, 20, 19]. Luckily for these methods, locality is not required for the purpose of deconvolution, and hence constant kernels suffice as input for the Wiener filter [18].

For our purpose of 2D US simulation, however, these methods do not work well. Convolution-based US simulation demands a smoothly-varying PSF to achieve the realism of an actual ultrasound image, and to teach aspiring sonographers the subtleties and effects of ultrasound beamforming on the image formation. The PSF varies not only with transducer geometry and acquisition settings, but it also changes locally as a function of depth (e.g., for a focused beam), and on a point-per-point basis as an effect of the underlying tissue. Hence a globally constant, or even a piece-wise constant PSF does not capture the complexity of a real continuous PSF distribution as a function of position.

We herein introduce a novel cepstrum-domain algorithm to approximate the PSF *locally* from an input US image to be used in simulations. Our goal is to (robustly) estimate *beam profiles* from actual images in order to use those later in common convolution-based (similarly, as well, in ray-tracing based) image simulation for training. Assuming separability of the PSF, our algorithm avoids the challenging problem of cepstrum-based estimation in 2D. Instead, we achieves robustness by sampling and combining many 1D cepstrum measurements via interpolation. Our estimated PSF can be subsequently used for simulation, without any manual modeling effort needed for this important aspect of ultrasound imaging. We demonstrate this in simulated and in-vivo images.

2 PSF Estimation from Image Data

In the typical convolution model of ultrasound speckle [2, 13, 12], the reflective image intensity $r(x, y)$ results from the convolution of a tissue model $g(x, y)$ with PSF $h(x, y)$ given noise n, i.e.

$$r(x, y) = g(x, y) * h(x, y) + n \tag{1}$$

where x denotes the lateral and y the axial transducer axes. Commonly, $h(x, y)$ is approximated by a periodic signal of acquisition center-frequency f_c modulated by a Gaussian, e.g. in [5, 4]. PSF is then of the form

$$h(x, y) = e^{-\frac{x^2}{\sigma_x^2} - \frac{y^2}{\sigma_y^2}} \cos(2\pi f_c) \ , \tag{2}$$

which is a function that is separable to lateral and axial components. We use separability to efficiently estimate the axial and lateral h components *directly* from an US image, given as a spatial discretization $r[x, y]$ of radio-frequency (RF) data. While the additive noise n in Eq. 1 can be handled using standard filtering techniques, finding the PSF from an image of reflective intensities r requires the contribution of PSF h to be separated from the reflected echo g from the tissue.

Homomorphic filtering is a signal processing technique [9] for separating a Fourier domain signal into its components. Using this, the signals h and g in Eq. 1 can be decoupled in Fourier space as follows:

$$\log(\mathcal{F}(h * g)) = \log(H \cdot G) = \log H + \log G, \tag{3}$$

where $\mathcal{F}$ denotes the Fourier transform and the capitals represent Fourier transforms of signals. Since a given signal is not necessarily minimum phase, complex logarithm is employed [3], i.e. $\log H \cdot G = \log(R) = \log(|R|e^{j\phi R}) = \log|R| + j\phi(R)$, where $\phi(R)$ denotes the unwrapped phase of the signal.

The main assumption of homomorphic filtering is that H is a relatively smooth function in Fourier space, in comparison to the typically highly varying and discontinuous nature of tissue G. As such, the components of H can be separated from the components of G by using lowpass filtering in the so-called *cepstrum* domain. The cepstrum is defined as $c = \mathcal{F}^{-1}(\log R)$, and constitutes a complex function $c(n)$ of the so-called *quefrencies*. Ideally, the first few components of c (up to a cutoff) contain only the PSF components of the input image. Using inverse cepstrum transformation on this truncated cepstrum c' then gives an estimation of PSF, i.e.,

$$h \approx \mathcal{F}^{-1}(\exp(\mathcal{F}(c'))). \tag{4}$$

In practice, a perfect separation between components is often not achieved. Several strategies have been proposed to improve robustness by increasing the separation between H and G in the Fourier domain. We adopt the strategy of *exponential pixel weighting* [9, 23]. For each measurement location, each data point within a surrounding window is multiplied by a factor $w{=}\alpha^d$, where $\alpha < 1$ and d is the distance from the upper left corner. This ensures a monotonically lower influence of farther signal values to a measurement in Eq. 3. This windowing technique is used herein to compute localized but spatially-smooth cepstrum measurements.

For ultrasound, homomorphic filtering has been used in the context of US deconvolution for *image restoration* in 1D, 2D, and 3D [6, 18, 20, 19]. These face several challenges, however, since in-vivo tissue and clinical scans are corrupted

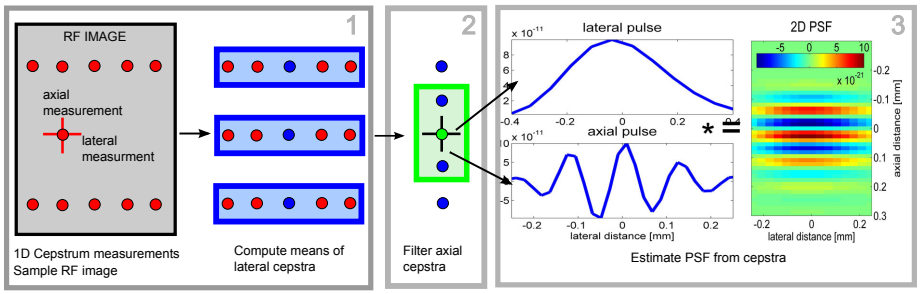

Fig. 1. Our method for robust estimation of a smoothly varying PSF.

by noise and contain artifacts and strong specular reflections hindering above approaches. For instance, a major challenge is due to the high sensitivity of phase unwrapping to noise, even more so in higher dimensions [10, 20, 19, 14]. Alternatives to phase unwrapping based on logarithmic derivatives exist [16, 18], but these are prone to severe aliasing artifacts. Instead, we propose the following.

3 Proposed Technique for Local PSF Estimation

As input to our method we use the raw radio-frequency (RF) data from a US scan. From an RF image $r[x, y]$, our algorithm computes a PSF $h[y]$ as a function of axial position y, while smaller lateral variations in x are ignored to employ averaging to increase estimation SNR. We describe below the three steps of our PSF estimation algorithm, which are also depicted in Figure 1.

Robust cepstrum estimation. The purpose of this step is to avoid instability and improve SNR of homomorphic filtering. Assuming a *separable* PSF, Eq. 3 is used twice per sample location to separately find the axial and lateral components of the cepstrum, respectively. Phase unwrapping can then be reduced to a 1D problem in either direction, which can be solved efficiently. Noise-corrupted phase unwrapping in 1D can still cause a corrupted cepstrum measurement, which would negatively influence the following steps. Fortunately, a potentially corrupted measurement can be detected from cepstrum values $c(n)$ as follows: While $c(1)$ encodes the overall image brightness similar to a DC component [10], $c(2)$ and $c(3)$ influence the shape of the estimated pulse. Suggestions for plausible cepstrum values and their interpretation are described in detail in the cepstrum literature, e.g. for $c(2)$ in [20]. Based on these, we empirically defined valid cepstrum measurements as $2 \leq |c(2)| \leq 6$ and $|c(2)| \leq |c(3)|$. We use these constraints as an outlier test, such that only the cepstra $\bar{c}$ that pass this test are employed in the following steps.

For each axial index y we compute a set of *local* cepstrum measurements $c\{[y_i]\}$, separated by lateral sampling distance δ (in our implementation δ=4 RF lines/pixels), depicted as red dots in Figure 1. We then compute both axial and lateral cepstra for each such sample point y_i, by giving importance only

to local neighborhood via exponentially weighted windowing. As the cepstrum $c[y]$ at a given arbitrary axial position y, we compute the arithmetic mean over valid cepstra $\bar{c}\{[y_i]\}$. Following this, we also average $c[y]$ over lateral measurements (depicted by blue dots in Figure 1), to remove lateral PSF variation while preserving and estimating its axial variation.

Axial filtering in cepstrum domain. A global or piecewise-constant PSF were proposed in previous works [6, 18, 20, 19]. Global PSF for the entire image is not a viable option for simulation, since PSF varies significantly in the axial direction and mimicking this is essential for a plausible simulation. A piece-wise constant (PWC) PSF approximation leads to discontinuities in the simulated image; and a simple interpolation of such PWC $h[y]$ in the *spatial* domain would not give a properly defined PSF, due to the frequency component of h. It was proposed in [21] to avoid image discontinuities due to discrete PSF kernels by running several simulations using different PSFs and merging resulting images in a weighting scheme. Alternatively, we use a filtering of axial cepstrum measurements $c[y]$ to obtain a smoothly varying function in the cepstrum domain, which subsequently can be transformed into a smoothly varying $h[y]$. A Gaussian window of standard deviation σ is applied on $c[y]$, where σ corresponds to an empirically set scale of expected PSF variation. Each value is then weighted by the number of valid cepstra $\bar{c}\{[y_i]\}$. The filter width n was set to 256 samples in our implementation, corresponding to $\approx 5\,\text{mm}$ for given sampling frequency. A $\sigma = 80$ RF samples (corresponding to a 3σ range of $\approx 4.6\,mm$) results in a successful trade-off between smoothing and variations.

PSF estimation from cepstrum. We compute the PSF $h[y]$ from $c[y]$ as follows. For each $h[a]$, we recover the lateral and axial pulse profiles by applying the inverse transformation from Eq. 4 to the truncated cepstrum $c'[a]$ after cutoff. The separable 2D PSF for each y is computed from the 1D pulses by convolution. A remaining problem is that Eq. 4 aligns h with the upper left corner of the image and hence does not constitute a proper impulse response. Assuming a pulse similar to Eq. 2, to get a centered PSF we first compute the envelope $E = \max(|\mathcal{H}(h)|)$ to remove the frequency component, and then center the maximum intensity $\max(E)$ in the lateral and axial directions. Since the envelope of an idealized PSF corresponds to a Gaussian, centering the maximum intensity also corresponds to centering the mean of the signal.

4 Results and Discussion

To find the ideal value of the cepstrum cutoff, using $1/6^{th}$ of the PSF *Full-Width at Half-Maximum* (FWHM) was recommended as a rule of thumb in the literature [18]. FWHM is the extent of a pulse where its intensity is half of its maximum value. In our implementation, we permanently fixed the lateral and axial cutoff to the first 4 and 5 quefrencies of c, respectively. The parameter α for exponential weighting, typically in the range of $[0.965, 0.995]$ [23], was set to 0.975 for all experiments. Figure 2 demonstrates local PSF estimation from a FieldII-simulated image (a) as input. For simulation, a 6.6 MHz linear transducer

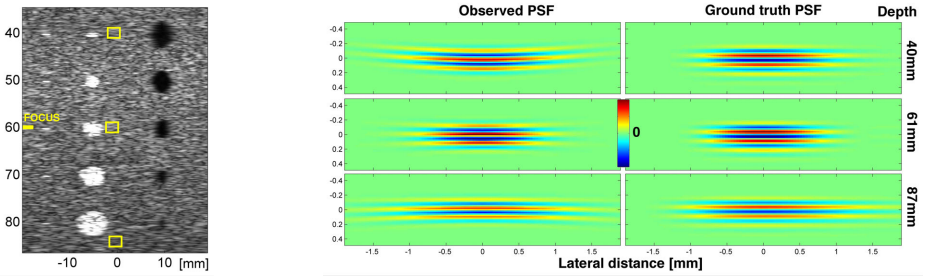

(a) Input image. (b) PSF comparison for 3 axial positions.

Fig. 2. Comparison of FieldII-simulated PSF and estimated PSF for a Cyst phantom.

with sampling frequency of 40 MHz and a width of 40 mm was used with a single transmit focus. To illustrate axial PSF variation, fixed receive focus points were used. A qualitative comparison of the FieldII PSF with the PSF estimated by our method in Figure 2(b) demonstrates an excellent agreement. Table 1 gives a numerical comparison of FWHM from simulated and estimated PSF at the illustrated three depths, which shows that the estimated values are in good agreement with the FWHM of the FieldII PSF, with differences $< 15\%$. Added Gaussian noise affects our method minimally; up to a noise level of 40 dB, where significant errors are observed.

Figure 3(a) visually compares FWHM for different values of axial filtering parameter σ. This illustrates our method in the case of PSF discontinuities in the original beam profile, which are caused by using multiple receive focus points equally-spaced with 20 mm separations. Despite the discontinuities, our method can faithfully approximate the original FHWM values and the general shape of the curve. While there is certain variation among the methods, they all converge to similar values in the far field. The lateral spread of local PSF, obtained as the aggregation of a fine discretization of local PSF envelopes placed along a vertical line, is shown in Fig 3(b) and called herein *beam shape*. It demonstrates that the estimated PSF is a smoothly varying function and in good agreement with FieldII simulation. Figure 3(c-d) show results for dynamic receive focusing,

Table 1. FWHM of estimated and FieldII-simulated PSFs, and the normalized errors.

Depth [mm]	40.4	60.6	86.6	40.4	60.6	86.6	40.4	60.6	86.6	40.4	60.6	86.6
FWHM	Lateral [mm]			Axial [mm]			Lat. error [%]			Ax. error [%]		
Noise-free	1.38	1.18	1.90	.262	.263	.258	0	7	0	6	**11**	5
70 dB noise	1.36	1.18	1.89	.263	.263	.257	1	7	0	1	**11**	4
50 dB noise	1.23	1.11	1.55	.244	.240	.210	**21**	1	13	1	2	19
40 dB noise	0.52	0.62	0.48	.194	.185	.142	**167**	79	291	26	27	73
Ground-truth	1.38	1.11	1.89	.246	.234	.246	0	0	0	0	0	0

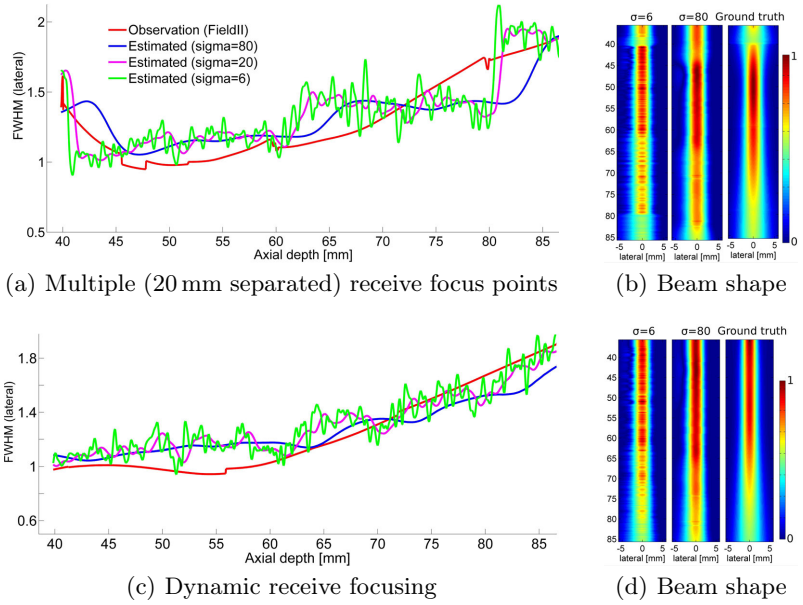

(a) Multiple (20 mm separated) receive focus points (b) Beam shape

(c) Dynamic receive focusing (d) Beam shape

Fig. 3. Full-Width-at-Half-Maximum (FWHM) of PSF over entire axial range of cyst phantom for 3 levels of axial filtering and two types of receive beam-forming; together with corresponding (lateral) beam shapes. The transmit focus is fixed at 60 mm in both cases.

where PSF variations are smaller. In this case, a better estimation accuracy is indicated by our results.

Figure 4 uses the estimated PSF for convolution-based simulation. In this example, the continuous set of $100K$ scatterers from a FieldII cyst phantom was discretized on a scatterer grid of 2701×1024 pixels. This map was convolved with the PSF estimated from FieldII simulation, where the simulated image should ideally be equivalent to the FieldII image. As baseline comparison, we used a technique form deconvolution literature, in which PSF estimation has most commonly been investigated. In particular, we approximate the PSF by (piecewise-)constant kernels; two in our case for the near and the far fields, c.f. Figure 4(b). The discontinuity between the two PSF kernels can be seen clearly as artifacts in the speckle pattern around 60 mm depth, making this method a poor choice for simulation. Conversely, the proposed PSF estimation method in Figure 4(c) exhibits a smoothly varying speckle appearance. Our method is visually in good agreement with the original image in Figure 4(d), with a focus sharper near 60 mm. For the anechoic cyst at 60mm, we computed contrast-to-noise ratio (CNR) as an indicator for visibility of pathology. Using $\mathrm{CNR}=\frac{|\mu_{I_1}-\mu_{I_2}|}{\sigma_{I_1}+\sigma_{I_2}}$, where I_1 and I_2 denote B-Mode pixel intensity values of the cyst and the surrounding tissue, respectively, resulted in 1.05 dB for piecewise-constant PSF estimation and 1.16 dB for our local PSF estimation, which is

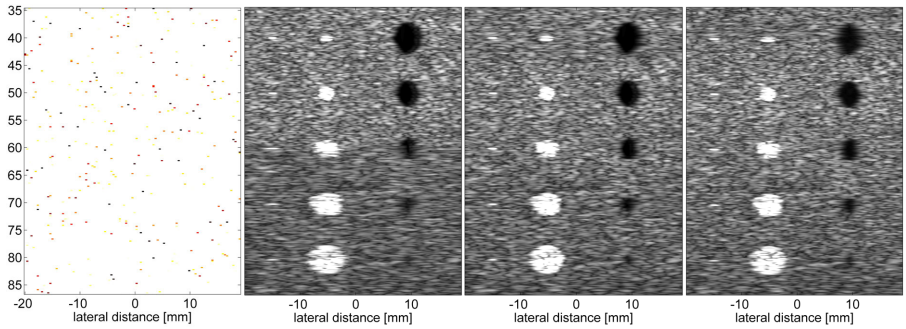

(a) Scatterer map (b) PWC PSF (c) Local PSF (d) Ground-truth

Fig. 4. Convolution-based simulation for the cyst phantom: (a) Discretized scatterers, 100× downsampled; (b) using 2-part piecewise-constant PSF with near- and far-field parts; (c) proposed local PSF estimation with σ=80; (d) ground-truth FieldII image.

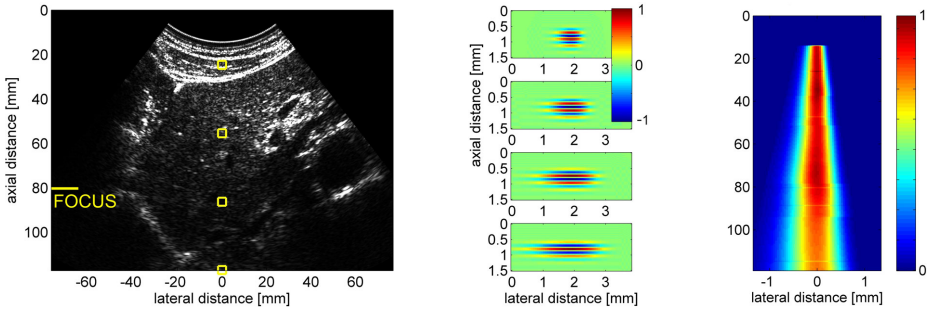

(a) Input image (RF envelope) (b) Sample PSF (c) Beam shape

Fig. 5. (a) Liver scan acquired with a convex probe. (b) Samples of the estimated PSF at 4 depths. (c) Beam shape as the smooth (lateral) variation of local PSFs.

closer to the observed value of 1.15 dB and indicating a contrast drop (and hence potential mis-training) in the case of inadequate PSF.

Figure 5 shows the example of an in-vivo liver scan. The input image (shown as *envelope* image on the left without dynamic compression) was captured with a SonixTouch 4*DC*7-3/40 convex probe operating at 4.5 MHz with 20 MHz sampling frequency and a transmit focus placed at 80 *mm*. The middle image shows estimated PSF at four depths marked in the left image. Note that since the estimation is performed in the pre-scan-converted RF data, convex images are also handled easily. The rightmost image depicts the continuous beam shape. As expected for a convex probe, it exhibits an almost linear increase of the beam width, where the focus is also discernible. The run time of the PSF estimation for this image was 13 minutes, in MATLAB with an Intel i7-4900MQ 2.8 GHZ CPU with 24 GB memory.

Discussion. Compared to earlier PSF estimation works such as [14, 18], our 3-stage approach has the most similarities to methods on separable deconvolution [1, 22], with some important differences: For the actual deconvolution, these earlier works simply use an averaged global kernel, whereas we employ additional local information exploiting separability. In contrast to our method, these previous methods make a single axial/lateral cepstrum measurement per axial/lateral scanline. As a result, they can capture lateral variation of the PSF w.r.t. image depth, but *not* the axial variation. Although the latter is potentially less pronounced than the former, it nevertheless still influences speckle statistics [15]. Instead, our algorithm first employs averaging in lateral direction followed by axial filtering, hence taking into account both lateral and axial components for each axial position. This allows us to robustly capture variation in *both* lateral and axial PSF components. A potential limitation of our method is that RF images are not accessible on most commercial ultrasound systems. Furthermore, to achieve simulation realism, not only the PSF but also the (proprietary) image post-processing steps should match those of a commercial system.

5 Conclusions

We have hereby presented a method to estimate PSF and its spatial variation from ultrasound images. This is to be used in US training simulation of linear and convex transducers. Despite several studies on both PSF estimation and convolution-based simulation, these fields have not been fused yet. We believe that both (convolution-based) US simulation and other potential uses of US PSF are of significant interest to medical ultrasound community. As evaluation, we presented visual and numerical comparisons of the acquired PSF with the PSF from numerical simulations. We also demonstrated an example of estimating PSF and the beam shape from a 2D in-vivo image. A 3D extension is to be studied in future work. This work was supported by the Swiss Commission for Technology and Innovation (CTI).

References

1. Abeyratne, U.R., Petropulu, A.P., Reid, J.M.: Higher order spectra based deconvolution of ultrasound images. IEEE Transactions on Ultrasonics, Ferroelectrics, and Frequency Control 42(6), 1064–1075 (Nov 1995)
2. Bamber, J.C., Dickinson, R.J.: Ultrasonic b-scanning: a computer simulation. Physics in Medicine and Biology 25(3), 463 (1980)
3. Bhanu, B., McClellan, J.H.: On the computation of the complex cepstrum. IEEE Transactions on Acoustics, Speech and Signal Processing 28(5), 583–585 (Oct 1980)
4. Bürger, B., Bettinghausen, S., M., R., Hesser, J.: Real-time gpu-based ultrasound simulation using deformable mesh models. IEEE Trans. Med. Imaging 32(3), 609–618 (2013)
5. Gao, H., Choi, H., Claus, P., Boonen, S., Jaecques, S., Van Lenthe, G., Van der Perre, G., Lauriks, W., D'hooge, J.: A fast convolution-based methodology to simulate 2-d/3-d cardiac ultrasound images. IEEE Transactions on Ultrasonics, Ferroelectrics, and Frequency Control 56(2), 404–409 (2009)

6. Jensen, J., Leeman, S.: Nonparametric estimation of ultrasound pulses. IEEE Transactions on Biomedical Engineering 41(10), 929–936 (Oct 1994)
7. Jensen, J., Mathorne, J., Gravesen, T., Stage, B.: Deconvolution of in vivo ultrasound b-mode images. Ultrasonic Imaging 15(2), 122 – 133 (1993)
8. Jensen, J.A.: Deconvolution of ultrasound images. Ultrasonic Imaging 14(1), 1 – 15 (1992)
9. Kobayashi, T., Imai, S.: Spectral analysis using generalized cepstrum. IEEE Transactions on Acoustics, Speech and Signal Processing 32(5), 1087–1089 (Oct 1984)
10. Lee, J.K., Kabrisky, M., Oxley, M.E., Rogers, S.K., Ruck, D.W.: The complex cepstrum applied to two-dimensional images. Pattern Recognition 26(10), 1579–1592 (1993)
11. Mattausch, O., Goksel, O.: Scatterer reconstruction and parametrization of homogeneous tissue for ultrasound image simulation. In: IEEE EMBC. pp. 6350–6353 (Aug 2015)
12. Meunier, J., Bertrand, M.: Ultrasonic texture motion analysis: theory and simulation. IEEE Trans. Med. Imaging 14(2), 293–300 (1995)
13. Meunier, J., Bertrand, M., Mailloux, G.: A model for dynamic texture analysis in two-dimensional echocardiograms of the myocardium. SPIE 0768, 193–200 (1987)
14. Michailovich, O., Adam, D.: Phase unwrapping for 2-d blind deconvolution of ultrasound images. IEEE Transactions on Medical Imaging 23(1), 7–25 (Jan 2004)
15. Oosterveld, B., Thijssen, J., Verhoef, W.: Texture of b-mode echograms: 3-d simulations and experiments of the effects of diffraction and scatterer density. Ultrasonic Imaging 7(2), 142–160 (1985)
16. Oppenheim, A.V., Schafer, R.W., Buck, J.R., et al.: Discrete-time signal processing, vol. 2. Prentice-hall Englewood Cliffs (1989)
17. Reis, G., Lappe, B., Kohn, S., C.Weber, Bertram, M., Hagen, H.: Towards a virtual echocardiographic tutoring system. In: Visualization in Medicine and Life Sciences, pp. 99–119. Springer Berlin (2008)
18. Taxt, T.: Restoration of medical ultrasound images using two-dimensional homomorphic deconvolution. IEEE Trans. UFFC 42(4), 543–554 (July 1995)
19. Taxt, T.: Three-dimensional blind deconvolution of ultrasound images. IEEE Trans. UFFC 48(4), 867–871 (July 2001)
20. Taxt, T.: Comparison of cepstrum based methods for radial blind deconvolution of ultrasound images. IEEE Trans. UFFC 1417(44), 666–674 (1997)
21. Varray, F., Liebgott, H., Cachard, C., Vray, D.: Fast simulation of realistic pseudo-acoustic nonlinear radio-frequency ultrasound images. In: 2014 IEEE International Ultrasonics Symposium. pp. 2217–2220 (Sept 2014)
22. Wan, S., Raju, B.I., Srinivasan, M.A.: Robust deconvolution of high-frequency ultrasound images using higher-order spectral analysis and wavelets. IEEE Trans. on Ultrasonics, Ferroelectrics, and Frequency Control 50(10), 1286–1295 (Oct 2003)
23. Yamada, I., Sakaniwa, K.: An optimal design of homomorphic deconvolution system. In: IEEE Symposium on Circuits and Systems. pp. 1344–1349 (May 1989)